

Nanoscale cuticle density variations correlate with pigmentation and color in butterfly wing scales

Anupama Prakash^{1†§}, Deepan Balakrishnan^{2†}, Benedikt J. Daurer^{3†}, Cédric Finet⁴, Ying Chen Lim⁴, Zhou Shen⁴, Pierre Thibault⁵, N. Duane Loh^{2,4*}, and Antónia Monteiro^{1*}

Affiliations:

¹Department of Biological Sciences, National University of Singapore, Singapore.

²Center for Bioimaging Sciences, National University of Singapore, Singapore 117557.

³Diamond Light Source, Harwell Science & Innovation Campus, Didcot OX11 0DE, UK.

⁴Department of Physics, National University of Singapore, Singapore 117551.

⁵Università degli Studi di Trieste, Trieste 34127, Italy.

†These authors contributed equally to this work.

§Current address: School of Biosciences, Faculty of Science, University of Sheffield, Sheffield S10 2TN, UK.

*Corresponding authors. Email: duaneloh@nus.edu.sg, antonia.monteiro@nus.edu.sg

Abstract: How pigment distribution correlates with cuticle density within a microscopic butterfly wing scale, and how both impact final reflected color remains unknown. We used ptychographic X-ray computed tomography to quantitatively determine, at nanoscale resolutions, the three-dimensional mass density of scales with pigmentation differences. By comparing cuticle densities with pigmentation and color within a scale, we determine that the lower lamina structure in all scales has the highest density and lowest pigmentation. Low pigment levels also correlate with sheet-like chitin structures as opposed to rod-like structures, and distinct density layers within the lower lamina help explain reflected color. We propose that pigments, in addition to absorbing specific wavelengths, can affect cuticle polymerization, density, and refractive index, thereby impacting reflected wavelengths that produce structural colors.

One-Sentence Summary: X-ray ptycho-tomography reveals density and structural variations in butterfly scale cuticles that correlate with pigmentation and color variations.

A detailed examination of the distribution of various matrix components within complex tissues, including proteins and pigments, has often led to a better understanding of their colour and other material properties (1–3). Some of the main components found in arthropod cuticles are chitin fibers embedded in a matrix of cuticular proteins and tyrosine-derived pigment molecules, secreted by the underlying cells (4–7). Variations in the chemical composition of these molecules and their organization within the layered matrix affect the properties and structure of the cuticle (6, 8–13). However, in the case of microscopic butterfly scales, which are the cuticular skeletons of single cells, little work has been done to explore how cuticle composition varies with scale morphology and color.

Butterfly scales owe their brilliant colors to the way that cuticle is patterned during development to produce non-pigmentary structural colors through light interference and diffraction (14–17). As the scale grows, cuticle is secreted to the outside of the cell membrane to produce two main cuticular surfaces connected via pillars or trabeculae: an upper lamina that is often intricately nanostructured and, a flat, sheet-like lower lamina (18, 19). Both upper and lower laminae of the scale can produce structural colors, but variations in just the lower lamina thickness are often sufficient to produce a large range of colors via thin-film interference (20). It has recently become apparent, however, that optical models that predict

structural colors from the physical dimensions of cuticle alone, assuming a homogeneous chitin matrix, are failing to capture the true color of the scales (20).

In addition, investigations into the genetics of butterfly scale development have identified a complex interplay between scale morphology and pigmentation (20–22). Pigments, such as melanins, are often deposited in the cuticular mass of the scale, and knockouts of two melanin pathway genes in *Bicyclus anynana* butterflies led to decreased pigmentation levels in wing scales but also impacted scale structures (21). In *yellow* crispants, an ectopic cuticular film was retained in the upper structures of black scales, closing the normally open ‘windows’ (Fig 1A, E), whereas in *Dopa Decarboxylase (DDC)* crispants, sheet-like trabeculae extended between the two laminae in place of pillar-like trabeculae (21). Similar interactions between scale structure and coloration were observed in *Junonia* butterflies where *optix* crispants led to a brown to blue scale transformation with simultaneous decrease in pigmentation and increase in the lower lamina thickness (20).

To better understand the influence of material composition, at nanoscale resolutions, on butterfly scale structure and their macroscopic optical properties, we utilized a range of techniques from microspectrophotometry, scanning and transmission electron microscopy (SEM/TEM) and ptychographic X-ray computed tomography (PXCT) (23–25). We characterized how relative pigmentation differences and mass density distributions within different scale sub-structures affected scale color. In particular, we demonstrate the application of PXCT for estimating quantitative mass densities of scale sub-structures at nanoscale resolution. These measurements revealed density differences between the two laminae of the scale. Further, distinct density layers within the lower lamina, suggest that spatial variations in pigments or cuticle proteins within the scale might affect how light travels through or bounces off cuticular surfaces. A multi-layered optical model taking into account these density variations predicts the experimental reflectance spectra of the scale more accurately than models based on a homogeneous cuticle matrix.

Scales are primarily pigmented in the upper lamina, and pigmentation correlates with changes in scale morphology

In this study, we compared two pairs of scales with differences in pigmentation in two species of nymphalid butterflies, *Junonia orithya* and *Bicyclus anynana*. In *J. orithya*, we compared the less pigmented blue cover scales of males with more pigmented brown female scales sampled from the same site (Fig 1B, D, Fig S1A, B). Similarly, in *B. anynana*, we compared cover scales from the *yellow* mutant line with the more pigmented black cover scales of wildtype, sampled around the large eyespot (Fig 1C, E, Fig S1C, D).

To determine the distribution of pigments between the scale’s upper and lower laminae, we observed the scales at high magnification and measured the reflectance and absorbance of single intact scales relative to scales with the upper laminae removed (Table S1). An absorbance spectrum of a scale measured by spectrophotometry is affected by the scale’s thickness and the density of color-absorbing pigments it contains. The thickness distributions of the upper and lower lamina from SEM and PXCT measurements (described below) enabled us to estimate the absorption spectra (Fig 1D’, E’), which is related to the pigment density (see Materials and Methods, Fig S2).

We found that most pigments were deposited in the upper lamina. This was because reflectance increased (Fig 1D’, E’) upon removal of the upper lamina and, the absorption spectra (Fig 1D”, E”) were higher for the upper laminae. Transmitted light images of intact scales immersed in clove oil showed that pigmentation was present in darkly stained ridges and

cross-ribs, which are the components of the upper lamina (Fig S1). In *B. anynana* scales, *yellow* mutant scales also exhibited a different absorption profile compared to wildtype scales reflecting a change in pigment composition upon knockout of the *yellow* gene (Fig 1E").

We then identified scale structural changes associated with changes in pigmentation levels in all four scales. To do this, we measured inter-ridge and cross-rib spacing (Fig 1A, red double-headed arrows), and the thickness of the lower lamina, using a combination of SEM and FIB-SEM (Fig 1F, G, Table S2). The blue scales of *J. orithya* males differed from the highly pigmented brown scales of females by having greater inter-ridge (lme, chisq = 336.12, p-value <0.001) and cross-rib distances (lme, chisq = 331.89, p-value <0.001) leading to larger 'windows' on the upper lamina (Fig 1F). In addition, the blue scales had a thicker lower lamina of ~190 nm as compared to the thinner lower lamina of ~158 nm in the brown scales (t-test, $t(4) = 8.12$, $p < 0.001$) (Fig 1F). This thicker, thin film of males produced a structural blue via constructive interference (20).

Among the *B. anynana* pair of scales, the *yellow* mutant scales displayed an ectopic cuticular film on the upper lamina closing all the windows (Fig 1E). TEM cross-sections indicated that the film was a very thin cuticle layer of about 10-20 nm in thickness (Fig S3). These *yellow* mutant scales also had larger inter-ridge distances (lme, chisq = 12.91, p-value <0.001) and a denser arrangement of cross-ribs (lme, chisq = 10.82, p-value ≤ 0.001) relative to wildtype scales, as reported previously in (21) (Fig 1G). The thickness of the lower lamina of the *B. anynana* wildtype scales was similar to the *yellow* mutant scales based on FIB-SEM measurements (t-test, $t(4) = 1.31$, p-value = 0.23) (Fig 1G).

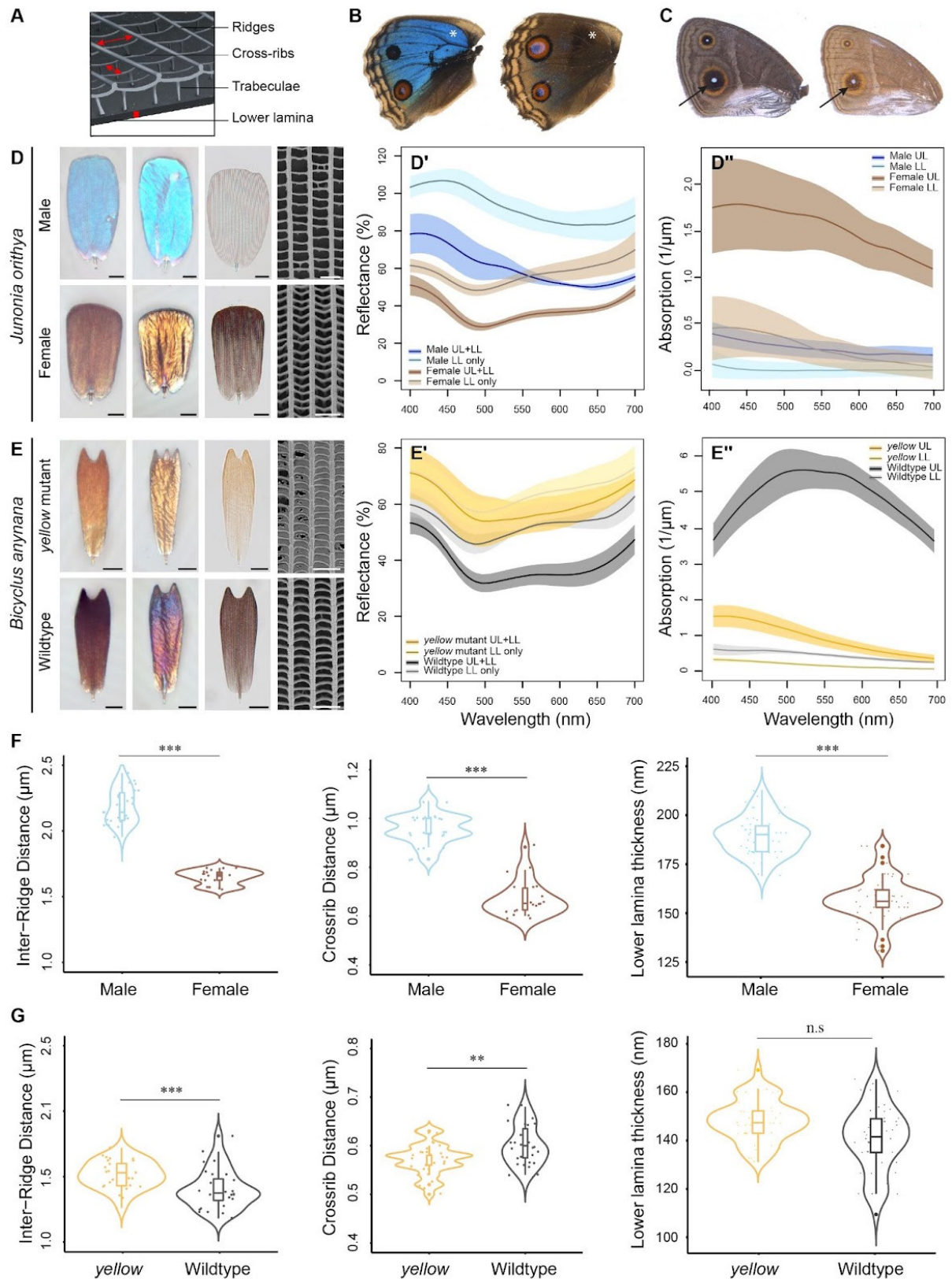


Fig. 1. Reflectance and absorption profiles and scale structure measurements of *Junonia orithya* and *Bicyclus anynana* scales. (A) Schematic of a wing scale showing a typical scale structure and the parameters measured (marked in red). (B) Dorsal hindwings of a *J. orithya* male (left) and female (right). White stars indicate the regions sampled. (C) Ventral forewings of a *B. anynana* wildtype (left) and *yellow* mutant (right). Black arrows indicate the regions

sampled. (D, E) Optical and SEM images of a male blue scale and a female brown scale of *J. orithya* (D), and a *yellow* mutant scale and wildtype scale of *B. anynana* (E). First column: Abwing images; Second column: Adwing images; Third column: Optical microscopy images of scales immersed in a chitin refractive index matching liquid (clove oil) that eliminates structural colors and measures pigmentary colors; Fourth column: SEM images of the upper lamina structures. Scale bars for the optical images are 20 μm and the SEM images are 2 μm . (D', E') Reflectance spectra of abwing *J. orithya* (D') and *B. anynana* (E') scales with intact upper and lower laminae (UL+LL) and scales with the upper laminae removed physically (LL only). (D'', E'') Estimated absorption spectra of *J. orithya* (D'') and *B. anynana* (E'') scales for their upper laminae (UL only) and lower laminae (LL only). (F) Violin plots of the inter-ridge distance, cross-rib spacing and the thickness of the lower laminae of male and female *J. orithya* scales. (G) Violin plots of the inter-ridge distance, cross-rib spacing and the thickness of the lower laminae of the *yellow* mutant and wildtype *B. anynana* scales. All boxplots show the median, inner and outer quartiles and whiskers up to 1.5 times the inter-quartile range. Asterisks indicate significant differences: ** $p \leq 0.01$, *** $p \leq 0.001$.

Cuticle density is highest in the lower laminae and is inversely correlated with pigmentation

To probe the distribution of materials within the scale sub-structures at nanoscale resolution, we imaged all four scale types using ptychographic X-ray computed tomography (PXCT). The PXCT reconstructions provided 3D distributions of electron densities (Fig 2; see Materials and Methods, Movies S1-S4) (26).

The 3D electron density maps showed both changes in density between upper and lower laminae as well as morphology between the pigmented and less pigmented scales of each species (Fig 2). In both *J. orithya* and *B. anynana* scales, the upper lamina of the less pigmented scale had sheet-like extensions from the cross-ribs as compared to the rod-like cross-ribs in the more pigmented scale (Fig 2, Fig S4, S5). The *B. anynana yellow* mutant scale also had disordered and bent trabeculae (Fig S5B, S6), that are not seen in the wildtype scale (Fig S5A, S6). Decreased pigmentation correlating with sheet-like cross-ribs suggests that the concentration and the type of pigments may determine structural differences between the scales, i.e., rod-like or sheet-like cross-ribs and straight or bent trabeculae, by promoting a particular type of chitin polymerization.

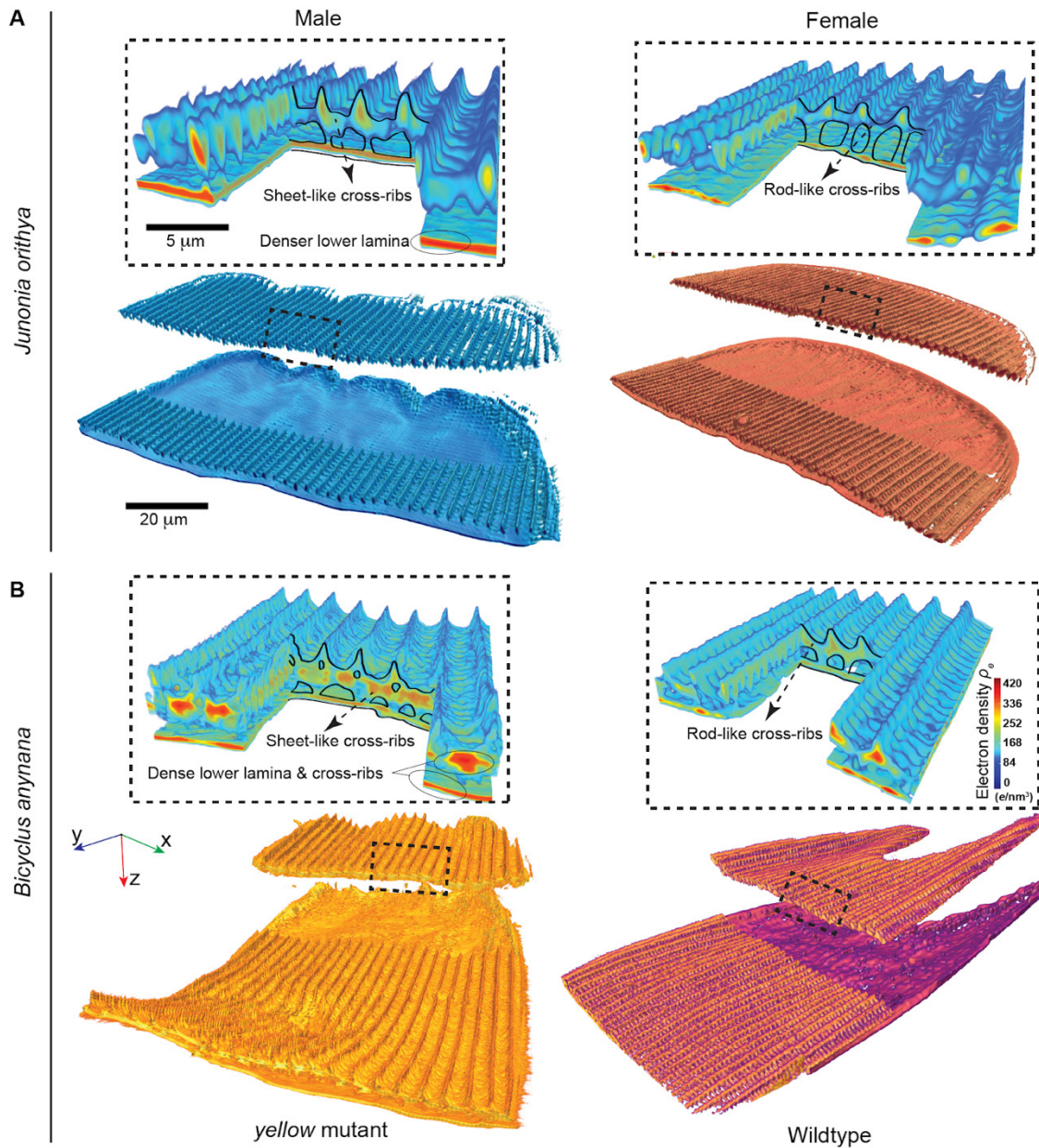


Fig. 2. Volume segmentation of 3D PXCT reconstructions of *J. orithya* and *B. anynana* scales. False color density contour renders of a (A) *J. orithya* male blue scale (left), and a female brown scale (right); and (B) a *B. anynana* yellow mutant scale (left) and a wildtype scale (right). The renders show digitally separated upper laminas, cut out from the rest of the scales. Black, dashed rectangles indicate the regions magnified for 3D electron density maps of the upper and lower lamina. Cross-sections along the ridges and across the ridges in the 3D heat maps show electron density variations within the scales. Annotated black lines outline the structural differences across scales.

To understand how the mass distribution varied between the different sub-structures of each scale, we computationally separated the PXCT volumes into upper and lower laminas, and then the upper lamina was further segmented into the three sub-structures: cross-ribs, ridges, and trabeculae based on their 1D mass density profiles (Fig 3A-D). Each such 1D profile shows the variation of mass densities along the abaxial-adaxial axis (top-bottom surface) of the scale, measured as voxels along the z -axis (Fig 3A-D, inset). We classified and segmented these 1D profiles as lower lamina, ridges, cross-ribs, trabeculae, or ectopic film on the upper

lamina (for *yellow* scales) (details in Materials and Methods) and calculated a boxplot of average mass densities within each structural class for the four scale types (Fig 3A'-D'). The mass densities within these sub-structures were calculated assuming each was made of only chitin monomers since their cuticular protein and pigment compositions are unknown. The contour-labels on the 2D density maps (scales seen from the top) validates the structural classification (Fig 3A''-D''). We caution that while PXCT reliably shows the *relative* densities between and within scales, the *absolute* density estimates reported here are lower bounds, owing to the well-known underestimation of densities in tomography of thin samples (27).

Compared to the other scales, the limited resolution (66.5 nm voxel side-length) and artifacts in the PXCT reconstructions of the complex architecture of the *yellow* mutant scale resulted in ambiguous class boundaries between the ectopic film on the upper lamina, cross-ribs, and trabeculae. Hence the segmentation for this scale type was carried out based on the relative distance from the lower lamina. Moreover, because the short trabeculae under the cross-ribs were thinner than the voxel side-length of our PXCT reconstructions, these features were less apparent in both the *B. anynana* and *J. orithya* pairs of scales.

For the most part, density was inversely correlated with pigmentation in both species. In all four scale types, the lower laminae (containing less pigment) were the densest (Fig 3A-A' – D-D', Fig 4). In the upper lamina, the density of the cross-ribs and trabeculae was higher in the lighter *yellow* scale compared to the darker wildtype scale in *B. anynana* (Fig 3C', D'). However, the opposite was observed in the upper lamina of *J. orithya*. Here, the densities of the ridges and cross-ribs were higher in the more pigmented female scale (Fig 3B'). Signatures from the ectopic film on the upper lamina of *yellow* scales, a feature that is present only in this scale type, were picked up in the regions between the sheet-like cross-ribs (Fig 3C''; yellow contours) but are likely underestimation of this lamina's density due to the large voxel size used.

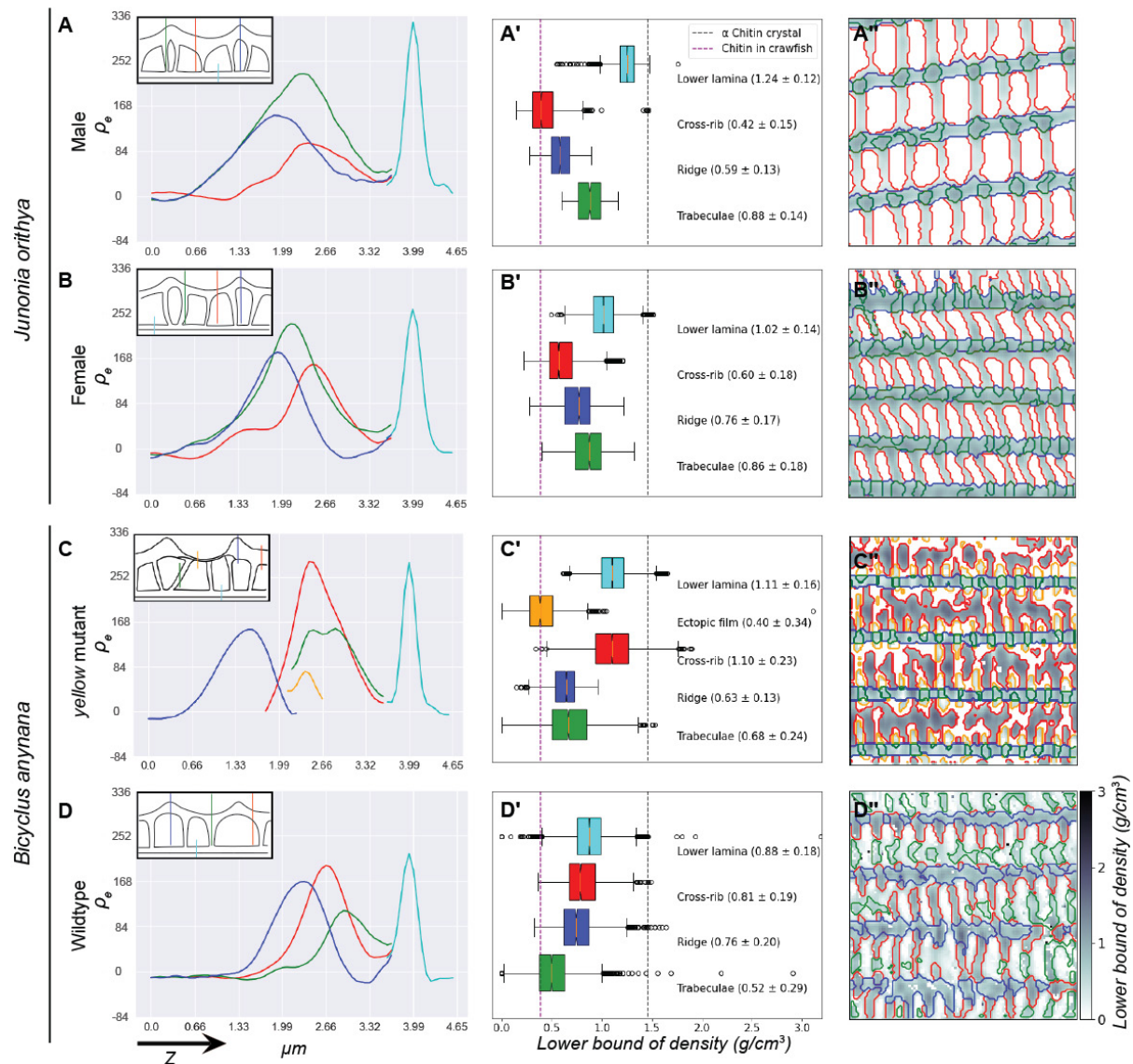


Fig. 3. Mass density estimations from the segmented volumes of *Junonia orithya* and *Bicyclus anynana* scales. Sub-volumes from the PXCT reconstructions are segmented and clustered based on mass distribution. (A-D) The mean electron density distribution along the z-axis (left to right: from abwing (upper) to adwing (lower)) of different upper lamina sub-structures with respect to the lower lamina of *J. orithya* male and female scales (A, B) and *B. anynana* yellow mutant and wildtype scales (C, D). Insets show a schematic view of the scales with colored lines marking the transected regions measured by the corresponding-colored curves. (A'-D') Box plots of the estimated mass densities clustered as lower lamina, cross-ribs, ridges and trabeculae reveal density variations across the scale sub-structures within each pair of differentially pigmented scales. Mass densities of α -chitin and chitin in crawfish are plotted to show the range of chitin densities reported in various organisms. (A''-D'') 2D mass density maps (upper lamina only) of the sub-volumes identified with colored contours.

The large mass density variations between different regions of each scale may be due to differences in how their constituent monomers pack together, e.g., lower density amorphous chitin to higher density crystalline alpha chitin. Chitin fibres are organized into diverse morphologies in cuticles of various natural systems (28, 29) and their organization and interactions with other molecules can change within different parts of the same structure (28,

30, 31). Chitin fibre organization can also change by modifications of the fibres such as deacetylation of chitin (32). We hypothesize that in the absence of pigments, or at low pigment levels, chitin packs into dense alpha-chitin crystals as observed in the lower laminas. Increasing pigment concentration frustrates the close-packing of chitin, which may lead to more amorphous and lower density forms of chitin-pigment mixtures, as observed in more pigmented lower laminas and in the upper laminas of all scales. It is possible that further increases in pigment concentrations beyond a threshold, may increase mass density due to the additional pigment mass. This would explain why the female upper lamina in *J. orithya*, in general, is denser than the male's.

Parameters other than pigmentation, however, may also regulate the variable cuticular density and morphology observed in the cross-ribs. Sheet-like cross-ribs developed in the less pigmented scales of both species (Fig S4, S5), but while the cross-ribs in the lighter *yellow B. anynana* mutant were denser than those in the darker wildtype scale (Fig 4C, D), the opposite was seen for the lighter *J. orithya* male cross-ribs relative to those of the darker female scale (Fig 4A, B). Additionally, in the *yellow* mutant scale, the sheet-like cross-ribs were deeper and tilted, appearing to fill in the 'window' spaces when viewed as a projection top-down (Fig 3C''; red contours, Fig S6, S7). It is possible that distinct cuticular proteins, or even different pigments, used by each species contribute to further regulate cuticle density and morphology of the cross-ribs.

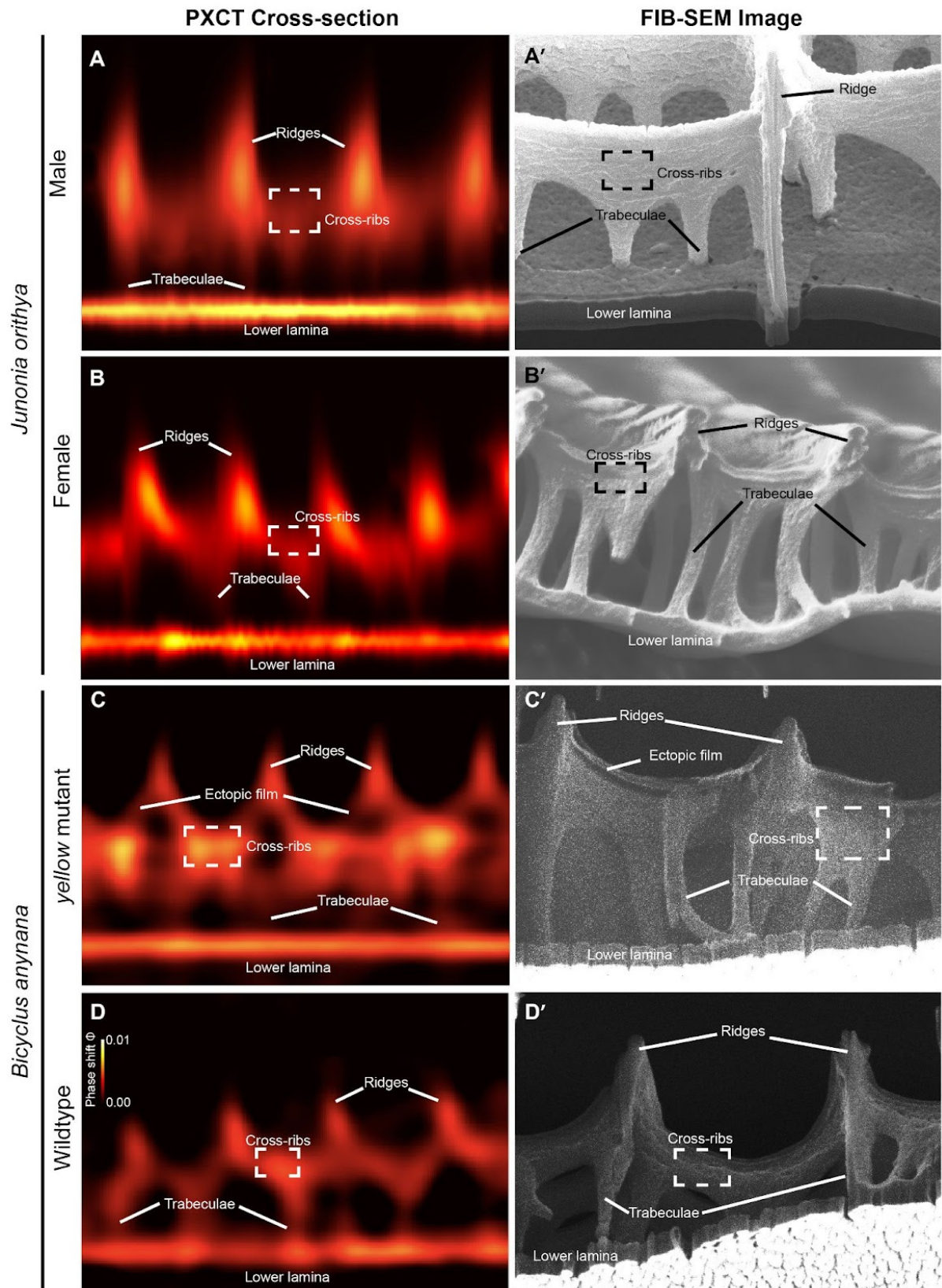


Fig. 4. Comparison of PXCT cross-sections, which include density distribution within the sub-structures, with the FIB-SEM images of *Junonia orithya* and *Bicyclus anynana* scales. (A-D) Cross-sections of the scales that are digitally cut from the PXCT reconstructions. (A'-D') FIB-SEM cross-sections of the respective scales.

Variation in cuticular densities within the lower lamina help model blue structural color

Our PXCT reconstructions indicated variation in cuticle densities across different sub-structures of the scale, but images of the lower lamina of a *J. orithya* male scale alone (Fig. 5B), indicated further density variations within this sub-structure. Such multi-layered lower laminae have been observed in TEM sections of other butterfly species (33). Thayer and colleagues reported that the sub-200 nm thick lower lamina of blue butterfly scales should either be composed of a high refractive index material or require a more complex model to match the modelled and experimental reflectance spectra (20). We confirmed that a single layer of chitin with refractive index 1.54 needs to be 220 nm thick to produce the observed blue reflectance spectra, which is far thicker than our SEM and TEM measurements (Fig 1F). To resolve this discrepancy, we used a three-layered thin-film interference model (for the lower lamina, LL) plus a transmission phase grating model (to model the ridges in the upper lamina, UL) to fit the reflectance curve measured from an intact *J. orithya* scale (UL+LL) as well as from only its lower lamina (LL only) (Fig. 5A). We constrained the total thickness of the three LL layers to match the average total thickness of the lower lamina measured in Fig. 1F. Our triple-layered lower lamina model fitted the broad spectral reflectance response of the scale better than the single-layered lower lamina model (Fig 5C). The respective optimal layer thicknesses and refractive indices of the lower lamina fitted in Fig 5A were: $t_{L1} = 18$ nm, $t_{L2} = 50$ nm, and $t_{L3} = 117$ nm; and $n_{L1} = 1.64$, $n_{L2} = 1.54$, and $n_{L3} = 2.1$. The higher refractive indices for the top and bottom layers correspond to darker (more dense) layers in the TEM image (Fig 5B).

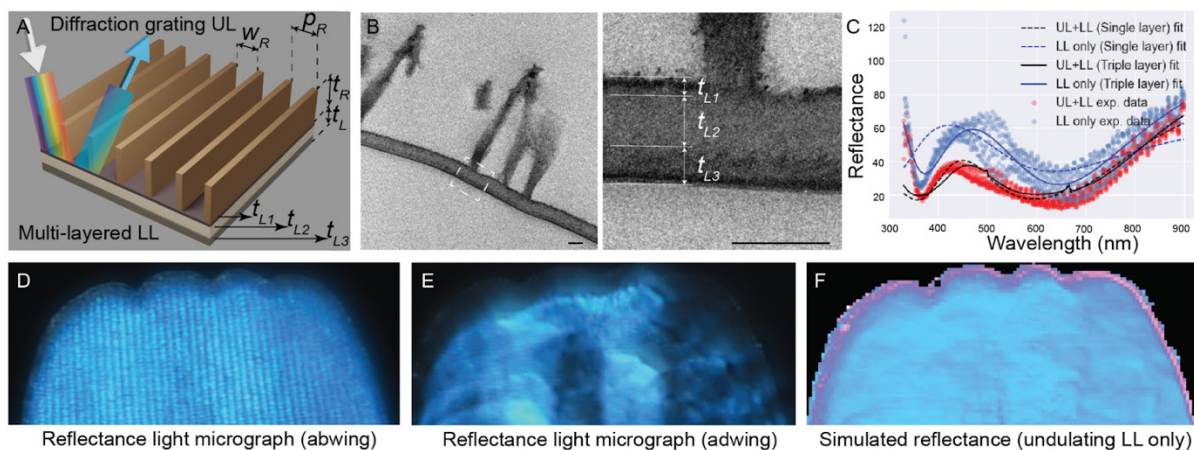


Fig. 5. A multi-layer thin-film interference model fit for reflectance spectra of *J. orithya* male blue scale. (A) A triple-layer model (layer thicknesses t_{L1} , t_{L2} , and t_{L3} and respective refractive indices n_{L1} , n_{L2} , and n_{L3}) was used for thin-film interference reflectance calculation (LL). A phase transmission diffraction grating model (UL) with window width (w), inter-ridge distance (p), ridge height (t) and refractive index (n) parameters, matching those of a male scale, were employed to simulate the effects of the UL. (B) TEM image of a blue scale of *J. orithya* male. The white rectangle indicates the region cropped for the magnified view. The lower lamina shows a less dense layer sandwiched between denser (darker) layers. Scale bar is 200 nm. (C) Reflectance spectra of a *J. orithya* male scale (intact upper and lower laminae (UL+LL) and the upper lamina physically removed (LL only)) with the single-layer thin-film interference model's best-fit spectra and the triple-layer thin-film interference model's spectra. (D, E) Epi-illumination light microscopy images of the abwing side (D) and the adwing side (E) of a *J. orithya* male blue scale. (F) A reflectance map simulated using the triple-layer model fit and an estimated tilt map from the PXCT reconstruction.

We also noticed that spatial color variations were present within a single scale. To investigate which factors led to this, we first modelled overall scale color taking into account the lower and upper laminae, and then subjected the same *J. orithya* male scale used in PXCT to high-resolution epi-illumination reflectance light microscope (Fig 5D, E). First, we applied our triple-layer model fit parameters from above to the lower lamina's spatially varying local tilt map extracted from the PXCT reconstruction. Here we assumed a constant thickness in the direction perpendicular to the lamina; hence the transverse variations of the lamina's apparent thickness as viewed from a fixed position either above or below the scale is entirely due to the lamina's changes in local tilt (i.e., undulations). We found that the simulated spatial variations in color reflectance across the scale's lower lamina (Fig 5F), without the upper lamina, were very sensitive to the changes in this local-tilt-induced apparent thickness (Movie S5 (GIF)). The upper lamina structures act as a color diffuser that spatially homogenizes the variations in color reflectance when viewed from the abwing direction (Fig 5D-F). Overall, these results indicate that the lower lamina of the *J. orithya* blue scale is not a uniform thin film but an undulating, multi-layered structure composed of materials of different refractive indices that impact the resultant structural colors. The color is very sensitive to tilt and lamina thickness, but color is spatially homogenized by the light-diffusing sub-structures of the upper lamina.

In conclusion, by studying two pairs of differentially pigmented scales in two different species of butterflies, we analysed the broad distribution of pigmentation and its influence on scale structure and structural color. We identified that scales, just like other bio-composite materials such as wood and bone (34), exhibit variations in morphologies, structure, and composition across nanometer to micrometer ranges. Such hierarchical structuring provides multifunctionality at various structural levels by a careful tuning of the material properties. We believe that the future to understanding the diversity of optical and mechanical properties of biomaterials will require 3D characterization of nanoscale variations in material composition, which quantitative density mapping techniques like PXCT, complementing the traditional imaging modalities, can help uncover.

References and Notes:

1. A. Miserez, T. Schneberk, C. Sun, F. W. Zok, J. H. Waite, The transition from stiff to compliant materials in squid beaks. *Science* (80-.). **319**, 1816–1819 (2008).
2. Craig, Hartley, The Arrangement and Structure of Feather Melanin Granules as a Taxonomic Character in African Starlings (Sturnidae) Author (s): Adrian J . F . K . Craig and Alex H . Hartley Published by : Oxford University Press Stable URL : [https://www.jstor.org/sta. 102, 629–632](https://www.jstor.org/sta.102,629-632) (1985).
3. C. M. Eliason, M. D. Shawkey, A photonic heterostructure produces diverse iridescent colours in duck wing patches. *J. R. Soc. Interface.* **9**, 2279–2289 (2012).
4. B. Moussian, C. Seifarth, U. Müller, J. Berger, H. Schwarz, Cuticle differentiation during *Drosophila* embryogenesis. *Arthropod Struct. Dev.* **35**, 137–152 (2006).
5. M. Y. Noh, S. Muthukrishnan, K. J. Kramer, Y. Arakane, Cuticle formation and pigmentation in beetles. *Curr. Opin. Insect Sci.* **17**, 1–9 (2016).
6. Y. Politi, L. Bertinetti, P. Fratzl, F. G. Barth, The spider cuticle: A remarkable material toolbox for functional diversity. *Philos. Trans. R. Soc. A Math. Phys. Eng. Sci.* **379** (2021), doi:10.1098/rsta.2020.0332.

7. J. H. Willis, Structural cuticular proteins from arthropods: annotation, nomenclature, and sequence characteristics in the genomics era. *Insect Biochem. Mol. Biol.* **40**, 189–204 (2010).
8. G. Xiong, X. Tong, T. Gai, C. Li, L. Qiao, A. Monteiro, H. Hu, M. Han, X. Ding, S. Wu, Z. Xiang, C. Lu, F. Dai, Body shape and coloration of silkworm larvae are influenced by a novel cuticular protein. *Genetics*. **207**, 1053–1066 (2017).
9. J. Liu, Z. Chen, Y. Xiao, T. Asano, S. Li, L. Peng, E. Chen, J. Zhang, W. Li, Y. Zhang, X. Tong, K. Kadono-Okuda, P. Zhao, N. He, K. P. Arunkumar, K. P. Gopinathan, Q. Xia, J. H. Willis, M. R. Goldsmith, K. Mita, Lepidopteran wing scales contain abundant cross-linked film-forming histidine-rich cuticular proteins. *Commun. Biol.* **4** (2021), doi:10.1038/s42003-021-01996-4.
10. R. Tajiri, N. Ogawa, H. Fujiwara, T. Kojima, Mechanical Control of Whole Body Shape by a Single Cuticular Protein Obstructor-E in *Drosophila melanogaster*. *PLoS Genet.* **13**, 1–26 (2017).
11. Y. Arakane, J. Lomakin, S. H. Gehrke, Y. Hiromasa, J. M. Tomich, S. Muthukrishnan, R. W. Beeman, K. J. Kramer, M. R. Kanost, Formation of rigid, non-flight forewings (Elytra) of a beetle requires two major cuticular proteins. *PLoS Genet.* **8** (2012), doi:10.1371/journal.pgen.1002682.
12. M. Y. Noh, S. Muthukrishnan, K. J. Kramer, Y. Arakane, *Tribolium castaneum* RR-1 cuticular protein TcCPR4 is required for formation of pore canals in rigid cuticle. *PLoS Genet.* **11**, e1004963 (2015).
13. M. Y. Noh, K. J. Kramer, S. Muthukrishnan, M. R. Kanost, R. W. Beeman, Y. Arakane, Two major cuticular proteins are required for assembly of horizontal laminae and vertical pore canals in rigid cuticle of *Tribolium castaneum*. *Insect Biochem. Mol. Biol.* **53**, 22–29 (2014).
14. M. A. Giraldo, D. G. Stavenga, Brilliant iridescence of *Morpho* butterfly wing scales is due to both a thin film lower lamina and a multilayered upper lamina. *J. Comp. Physiol. A Neuroethol. Sensory, Neural, Behav. Physiol.* **202**, 381–388 (2016).
15. A. J. Parnell, J. E. Bradford, E. V. Curran, A. L. Washington, G. Adams, M. N. Brien, S. L. Burg, C. Morochz, J. P. A. Fairclough, P. Vukusic, S. J. Martin, S. Doak, N. J. Nadeau, Wing scale ultrastructure underlying convergent and divergent iridescent colours in mimetic *Heliconius* butterflies. *J. R. Soc. Interface.* **15** (2018), doi:10.1098/rsif.2017.0948.
16. P. Vukusic, R. Sambles, C. Lawrence, G. Wakely, Sculpted-multilayer optical effects in two species of *Papilio* butterfly. *Appl. Opt.* **40**, 1116 (2001).
17. A. Prakash, C. Finet, T. Das Banerjee, V. Saranathan, A. Monteiro, Antennapedia and optix regulate metallic silver wing scale development and cell shape in *Bicyclus anynana* butterflies. *Cell Rep.* **40** (2022), doi:10.1016/j.celrep.2022.111052.
18. A. Dinwiddie, R. Null, M. Pizzano, L. Chuong, A. Leigh Krup, H. Ee Tan, N. H. Patel, Dynamics of F-actin prefigure the structure of butterfly wing scales. *Dev. Biol.* **392**, 404–418 (2014).
19. H. Ghiradella, Light and color on the wing : butterflies and moths structural colors in. *Appl. Opt.* **30**, 3492–3500 (1991).
20. R. C. Thayer, F. I. Allen, N. H. Patel, Structural color in *Junonia* butterflies evolves by tuning scale lamina thickness. *Elife.* **9**, e52187 (2020).

21. Y. Matsuoka, A. Monteiro, Melanin Pathway Genes Regulate Color and Morphology of Butterfly Wing Scales. *Cell Rep.* **24**, 56–65 (2018).
22. L. Livraghi, J. J. Hanly, S. M. Van Bellghem, G. Montejo-Kovacevich, E. S. M. van der Heijden, L. S. Loh, A. Ren, I. A. Warren, J. J. Lewis, C. Concha, L. Hebberecht, C. J. Wright, J. M. Walker, J. Foley, Z. H. Goldberg, H. Arenas-Castro, C. Salazar, M. W. Perry, R. Papa, A. Martin, W. O. McMillan, C. D. Jiggins, Cortex cis-regulatory switches establish scale colour identity and pattern diversity in heliconius. *Elife.* **10**, 1–31 (2021).
23. M. Dierolf, A. Menzel, P. Thibault, P. Schneider, C. M. Kewish, R. Wepf, O. Bunk, F. Pfeiffer, Ptychographic X-ray computed tomography at the nanoscale. *Nature.* **467**, 436–439 (2010).
24. M. Holler, M. Guizar-Sicairos, E. H. R. Tsai, R. Dinapoli, E. Müller, O. Bunk, J. Raabe, G. Aepli, High-resolution non-destructive three-dimensional imaging of integrated circuits. *Nature.* **543**, 402–406 (2017).
25. S. Sala, D. J. Batey, A. Prakash, S. Ahmed, C. Rau, P. Thibault, Ptychographic X-ray computed tomography at a high-brilliance X-ray source. *Opt. Express.* **27** (2019), doi:10.1364/OE.27.000533.
26. A. Diaz, P. Trtik, M. Guizar-Sicairos, A. Menzel, P. Thibault, O. Bunk, Quantitative x-ray phase nanotomography. *Phys. Rev. B.* **85**, 20104 (2012).
27. G. Dougherty, D. Newman, Measurement of thickness and density of thin structures by computed tomography: A simulation study. *Med. Phys.* **26**, 1341–1348 (1999).
28. R. Chandran, L. Williams, A. Hung, K. Nowlin, D. LaJeunesse, SEM characterization of anatomical variation in chitin organization in insect and arthropod cuticles. *Micron.* **82**, 74–85 (2016).
29. D. Raabe, P. Romano, C. Sachs, H. Fabritius, A. Al-Sawalmih, S. B. Yi, G. Servos, H. G. Hartwig, Microstructure and crystallographic texture of the chitin-protein network in the biological composite material of the exoskeleton of the lobster *Homarus americanus*. *Mater. Sci. Eng. A.* **421**, 143–153 (2006).
30. D. Raabe, C. Sachs, P. Romano, The crustacean exoskeleton as an example of a structurally and mechanically graded biological nanocomposite material. *Acta Mater.* **53**, 4281–4292 (2005).
31. S. Sviben, O. Spaeker, M. Bennet, M. Albéric, M. Albéric, J. H. Dirks, J. H. Dirks, B. Moussian, P. Fratzl, L. Bertinetti, Y. Politi, Epidermal Cell Surface Structure and Chitin-Protein Co-assembly Determine Fiber Architecture in the Locust Cuticle. *ACS Appl. Mater. Interfaces.* **12**, 25581–25590 (2020).
32. R. Yu, W. Liu, D. Li, X. Zhao, G. Ding, M. Zhang, E. Ma, K. Y. Zhu, S. Li, B. Moussian, J. Zhang, Helicoidal organization of chitin in the cuticle of the migratory locust requires the function of the chitin deacetylase2 enzyme (LmCDA2). *J. Biol. Chem.* **291**, 24352–24363 (2016).
33. T. M. Trzeciak, B. D. Wilts, D. G. Stavenga, P. Vukusic, Variable multilayer reflection together with long-pass filtering pigment determines the wing coloration of papilionid butterflies of the nireus group. *Opt. Express.* **20**, 8877–8890 (2012).
34. J. W. C. Dunlop, P. Fratzl, Biological composites. *Annu. Rev. Mater. Res.* **40**, 1–24 (2010).

35. H. Connahs, E. J. Tan, Y. T. Ter, E. Dion, Y. Matsuoka, A. Bear, A. Monteiro, The yellow gene regulates behavioural plasticity by repressing male courtship in *Bicyclus anynana* butterflies. *Proc. R. Soc. B Biol. Sci.* 289, 20212665 (2022).
36. R Core Team, R: A Language and Environment for Statistical Computing (2021), (available at <https://www.r-project.org/>).
37. R. Maia, H. Gruson, J. A. Endler, T. E. White, pavo 2: New tools for the spectral and spatial analysis of colour in r. *Methods Ecol. Evol.* 10, 1097–1107 (2019).
38. C. A. Schneider, W. S. Rasband, K. W. Eliceiri, NIH Image to ImageJ: 25 years of image analysis. *Nat. Methods.* 9, 671–675 (2012).
39. J. Pinheiro, D. Bates, R-core, nlme: Linear and Nonlinear Mixed Effects Models (2021), (available at <https://svn.r-project.org/R-packages/trunk/nlme/>).
40. V. S. C. Kuppili, S. Sala, S. Chalkidis, A. M. Wise, A. D. Parsons, I. Zanette, C. Rau, P. Thibault, Ptychotomography at DLS Coherence Beamline I13. *J. Phys. Conf. Ser.* 849, 12031 (2017).
41. S. Cipiccia, D. Batey, X. Shi, S. Williams, K. Wanelik, A. Wilson, P. Martin, T. Scott, C. Rau, Multi-scale multi-dimensional imaging at I13-coherence branchline in diamond light source. *AIP Conf. Proc.* 2054, 50005 (2019).
42. C. Rau, U. Wagner, Z. Pešić, A. De Fanis, Coherent imaging at the Diamond beamline I13. *Phys. status solidi.* 208, 2522–2525 (2011).
43. N. Tartoni, G. Dennis, P. Gibbons, E. Gimenez, I. Horswell, J. Marchal, U. Pedersen, Z. Pesic, R. Plackett, C. Rau, R. Somayaji, J. Spiers, J. Thompson, B. Willis, C. Angelsen, P. Booker, S. Burge, J. Lipp, T. Nicholls, S. Taghavi, M. Thorpe, in 2012 IEEE Nuclear Science Symposium and Medical Imaging Conference Record (NSS/MIC) (2012), pp. 530–533.
44. J. Marchal, I. Horswell, B. Willis, R. Plackett, E. N. Gimenez, J. Spiers, D. Ballard, P. Booker, J. A. Thompson, P. Gibbons, S. R. Burge, T. Nicholls, J. Lipp, N. Tartoni, EXCALIBUR: a small-pixel photon counting area detector for coherent X-ray diffraction - Front-end design, fabrication and characterisation. *J. Phys. Conf. Ser.* 425, 62003 (2013).
45. M. Pham, A. Rana, J. Miao, S. Osher, Semi-implicit relaxed Douglas-Rachford algorithm (sDR) for ptychography. *Opt. Express.* 27, 31246–31260 (2019).
46. B. Enders, P. Thibault, A computational framework for ptychographic reconstructions. *Proc. R. Soc. A Math. Phys. Eng. Sci.* 472, 20160640 (2016).
47. W. van Aarle, W. J. Palenstijn, J. Cant, E. Janssens, F. Bleichrodt, A. Dabrovolski, J. De Beenhouwer, K. Joost Batenburg, J. Sijbers, Fast and flexible X-ray tomography using the ASTRA toolbox. *Opt. Express.* 24, 25129–25147 (2016).
48. N. Wadson, M. Basham, Savu: {A} Python-based, {MPI} Framework for Simultaneous Processing of Multiple, N-dimensional, Large Tomography Datasets. CoRR. abs/1610.0 (2016) (available at <http://arxiv.org/abs/1610.08015>).
49. M. Guizar-Sicairos, A. Diaz, M. Holler, M. S. Lucas, A. Menzel, R. A. Wepf, O. Bunk, Phase tomography from x-ray coherent diffractive imaging projections. *Opt. Express.* 19, 21345–21357 (2011).
50. N. T. Vo, M. Drakopoulos, R. C. Atwood, C. Reinhard, Reliable method for calculating the center of rotation in parallel-beam tomography. *Opt. Express.* 22, 19078–19086 (2014).

51. D. Gürsoy, Direct coupling of tomography and ptychography. *Opt. Lett.* 42, 3169–3172 (2017).
52. G.-H. Chen, J. Zambelli, N. Bevins, Z. Qi, K. Li, X-ray phase sensitive imaging methods: basic physical principles and potential medical applications. *Curr. Med. Imaging Rev.* 6, 90–99 (2010).
53. R. M. Kessler, J. R. J. Ellis, M. Eden, Analysis of Emission Tomographic Scan Data: Limitations Imposed by Resolution and Background. *J. Comput. Assist. Tomogr.* 8 (1984) (available at https://journals.lww.com/jcat/Fulltext/1984/06000/Analysis_of_Emission_Tomographic_Scan_Data_.28.aspx).
54. D. Y. K. Ko, J. R. Sambles, Scattering matrix method for propagation of radiation in stratified media: attenuated total reflection studies of liquid crystals. *J. Opt. Soc. Am. A.* 5, 1863–1866 (1988).
55. J. A. Brand Faria, A transmission phase grating analysis. *Microw. Opt. Technol. Lett.* 4, 224–227 (1991).

Acknowledgments: We thank Ms. Tan Suat Hoon and Mr. Sim Aik Yong of the Electron Microscopy Unit at the Yong Loo Lin School of Medicine for their service in preparing the TEM resin blocks and sections. We acknowledge Diamond Light Source for time on I13-1 under proposal MG23967-1. We thank Dr. Darren Batey and Dr. Silvia Cipiccia for technical support and Dr. Simone Sala for help with data processing during the PXCT measurements taken at the I13-1 beamline. We would also like to acknowledge the use of the High Performance Computing facilities at the Diamond Light Source for the processing of the PXCT data.

Funding:

National Research Foundation (NRF) Singapore, Competitive Research Program grants NRF-CRP20-2017-0001(AM), NRF-CRP25-2020-0001 (AM) and Investigatorship award NRF-NRFI05-2019-0006 (AM)

National University of Singapore Early Career Research Award (NDL)

European Research Council Consolidator Grant S-BaXIT (866026) (PT)

Author contributions:

Conceptualization: AP, BJD, NDL, AM

Methodology: AP, DB, BJD, PT, NDL, AM

Formal analysis: DB, BJD, YCL, ZS, NDL

Investigation: AP, DB, BJD, CF, NDL

Visualization: AP, DB, CF

Funding acquisition: AM, NDL, PT

Project administration: AM, NDL

Supervision: AM, NDL

Writing – original draft: AP, DB

Writing – review & editing: AP, DB, BJD, CF, PT, NDL, AM

Competing interests: Authors declare that they have no competing interests.

Data and materials availability: Custom code for X-ray ptycho-tomography 3D reconstruction volumetric data analysis and Optical modelling is available as a Jupyter notebooks <https://zenodo.org/record/7922543#.ZFzAa3bMK3A>. Cropped X ray reconstruction volumes used for the analysis and the corresponding results that are plotted in the manuscript are also included. All other data are available in the supplementary materials.

Supplementary Materials

Materials and Methods

Figs. S1 to S8

References (35–55)

Tables S1 to S2

Movies S1 to S5

Supplementary Materials for

Nanoscale cuticle density variations correlate with pigmentation and color in butterfly wing scales

Anupama Prakash, Deepan Balakrishnan, Benedikt J. Daurer, Cédric Finet, Ying Chen Lim, Zhou Shen, Pierre Thibault, N. Duane Loh, and Antónia Monteiro

Corresponding authors: duaneloh@nus.edu.sg, antonia.monteiro@nus.edu.sg

Materials and Methods

Specimens

Individuals of wildtype *Bicyclus anynana* butterflies were sampled from the stock population in the Monteiro lab. A mutant *yellow* line was generated by a CRISPR/Cas9 knockout of the gene *yellow* (35). Individuals of *Junonia orithya* were collected from Coney Island, Singapore (Permit No: NP/RP 14-063-2) and were placed in mesh cages with the host plant, *Asystasia gangetica*, to collect eggs. They were fed with 5% sugar water and additional sources of heat were added to elicit activity. Caterpillars were reared for one generation in a 27°C temperature-controlled room with a 12:12 hour light cycle and 65% humidity.

Optical imaging

Epi-illumination microscope images of individual scales were obtained with a 20x lens of a uSight-2000-Ni microspectrophotometer (Technospex Pte. Ltd., Singapore) and a Touptek U3CMOS-05 camera. Images at different depths were obtained and computationally stacked using Adobe Photoshop v 22.5.1 (Adobe, California, USA).

UV-VIS-NIR microspectrophotometry

Reflectance and absorbance measurements from individual scales were captured with a 20x objective from a ~2 µm sized spot using a uSight-2000-Ni microspectrophotometer (Technospex Pte. Ltd., Singapore). Illumination was from a Mercury-Xenon lamp (ThorLabs Inc., New Jersey, USA). Measurements were taken from five different scales of each type from one individual.

To remove the upper lamina and be able to measure spectra from the lower lamina only, scales were mounted onto a double-sided sticky tape. The upper lamina was scratched with a pin to break the ridges. Another double-sided sticky tape was used to separate the upper and lower laminas with the lower lamina attached to the sticky tape.

For the reflectance measurements, we used the sticky tape in air as a reference which is why reflectance is above 40% for the brown scales. For the absorbance measurements, the two laminas were separated in the same way as above using a double-sided sticky tape. A drop of clove oil (a refractive index matching fluid) was added on top and covered with a cover slip. A part of the tape with clove oil and coverslip was used as a reference for absorbance measurements. Analysis and spectral plots were done in R Studio 1.4.1106 with R 4.0.4 (36) using the R-package *pavo* (v 2.7) (37).

The reflectance of FIB-milled regions was captured with a Nikon TU Plan Fluor 100x objective (NA= 0.9). Samples were mounted on carbon tape and calibrated using an Avantes WS-2 reference tile made of white diffuse polytetrafluoroethylene. Each measurement was performed with an integration time of 100ms and an averaging of 10. Three technical replicates were performed and averaged.

Scanning electron microscopy (SEM) and scale measurements

Three to six individual scales were sampled from the different areas under study from five different individuals and placed on carbon tape. Samples were processed in one of two ways: a) sputter coated with gold using a JFC-1100 Fine Coat Ion Sputter (JEOL Ltd. Japan) and imaged using a JEOL JSM-6510LV scanning electron microscope (JEOL Ltd. Japan) or b) sputter coated with platinum using a JFC-1600 Auto Fine Coater (JEOL Ltd. Japan) and imaged using a JEOL JSM-6701F FESEM (JEOL Ltd. Japan).

All measurements were done using ImageJ (38). For inter-ridge distance measurements, five individual measures were taken for each scale and averaged. Cross-rib distances were calculated by measuring the number of cross-ribs per 15 μm .

Statistical analysis

Analyses were done on R Studio 1.4.1106 with R 4.0.4 (36). Since the datasets were hierarchical with many scales sampled from each individual, the differences in mean values of inter-ridge and cross-rib distances among the different comparisons were modeled using a linear mixed-effects model (LME). This type of model allows for fixed and random effects where we considered Sex (*J. orithya* male or female) and Type (*B. anynana* WT or *yellow* mutant) as fixed factors and scale nested within individual as a random factor. LME was run using the nlme package (v 3.1.152) (39). To address the violation of the homogeneity of variance in certain measurements, we used the 'varIdent' function in the nlme package to allow for different variance structures. Models were compared using the ANOVA function and best models were selected using AIC.

Focused ion beam scanning electron microscopy (FIB-SEM) and thickness measurements

Lower lamina thickness of all four scale types was measured using FIB-SEM. Measurements were corrected for tilt by dividing the values with $\sin 52^\circ$. Samples were first sputter-coated with platinum then milled at the centre of each scale using a gallium ion beam on a FEI Versa 3D. The following settings were used: beam voltage -8kV , beam current -12pA at a 52° tilt. Images were acquired with the following settings: beam voltage -5kV , beam current -13pA . Five scales were sampled from a single individual of each category. For each scale, ten measurements of thickness were taken along the cross-section of the lower lamina using Fiji (38).

To test the multilayered structure of the lower lamina in *Junonia* blue scales, we performed a series of milling at four different depths. The uncoated scale was placed on carbon tape with the lower lamina (adaxial side) facing up. For each condition, an area of $3 \times 3 \mu\text{m}$ was milled with a beam voltage set at 8kV and a beam current set at 6pA . We entered the expected z values (depth) in the software as 50, 100, 150 and 200 nm. Subsequently, to reflectance measurement, we estimated the exact value of z by performing a cross-section of the milled by FIB. The expected z values of 50, 100, 150 and 200 nm were adjusted to 43, 85, 132 and 166 nm, respectively.

Ptychographic X-ray computed tomography (PXCT)

In preparation for the tomographic X-ray imaging, the specimens of both *Junonia orithya* and *Bicyclus anynana* were fixed at the tip of a sharp needle (0.4 mm diameter at the base), which was then inserted into a 0.5 mm hole drilled at the center of a standard SEM specimen stub (12.5 mm diameter, 3.2 x 8mm pin). Additionally, the needle was glued to the stub at its base. The PXCT data was collected at the I13-1 Coherent Branchline (40–42) at the Diamond Light Source with a photon energy of 9.7 keV, similar to a previous experiment on butterfly scales (25). The sample plane was located ~14 mm downstream of the focal plane of the X-ray beam providing a defocused beam with a diameter of ~13 μm . Focusing was achieved using a Blazed Fresnel zone plate (courtesy of collaboration with C. David/PSI) with 400 μm diameter and 150 nm outer zone width. The data for the male specimen of *Junonia orithya* was collected with the Merlin detector, all other specimens were collected with the EXCALIBUR detector (43,44). Both detectors are based on Medipix3 arrays with 55 μm pixel pitch, and they were both located 14.65 m downstream of the sample plane. For each PXCT measurement, the specimen stub was mounted at the center of the translational and rotational sample stage and scanned transversally with a step size of 4 μm for 1250 equally spaced tomographic angles between 0° and 180° providing a ptychographic dataset for each tomographic angle. The ptychographic data was reconstructed using 1000 iterations of the semi-implicit Douglas-Rachford algorithm (45) with $\sigma = 0.5$ and $\tau = 0.1$ as implemented in the PtyPy framework (46). As a pre-processing step, all diffraction patterns were cropped to 512x512 pixels resulting in a reconstructed pixel size of 66.5 nm in the given experimental geometry, and a bad pixel mask (including hot, dead, inactive pixels) was used. The initial guess for the illumination was determined by collecting and reconstructing data from a Siemens star test target. For each specimen a tomographic volume was reconstructed based on the ptychographic phase projections using the filtered-back projection algorithm (Ram-Lak filter) from the ASTRA toolbox (47) as implemented in the Savu framework (48). Prior to the tomographic reconstruction, the phase projections were aligned along the vertical direction by correlating integrated vertical line profiles (49), and the center of rotation was determined using a simplified version of the method described (50) but with a manual search instead of the Fourier analysis. To improve the quality of the tomographic reconstructions, the volume was forward-projected to generate a set of synthetic phase projections. These synthetic phase images were compared against the original phase reconstructions while searching for an improved alignment in both the vertical and horizontal direction (49,51). The updated phase projections were subsequently put through the same tomographic reconstruction process as described above. This iterative alignment scheme was repeated 5 times providing a total of 4 three-dimensional electron density maps (Fig. 3).

Segmentation and density estimation

We used a series of computational techniques to process the reconstructed volumes from PXCT to extract quantitative data effectively. The reconstructed volumes were first rotated such that the lower lamina aligns flat (as possible) on the x - y plane. This rotation was performed using a combination of principal component analysis (PCA) on selected features of each scale. Each rotated scale was inspected to the the lower lamina was satisfactorily aligned to the x - y plane. Then we used a peak finding method to find the dense lower lamina along 1D z -axis phase profiles (i.e., constant x,y) of the 3D phase volume (i.e., electron density) obtained from PXCT. Once the lower lamina was located, they were digitally aligned in z to remove their local tilt variations. This alignment reduced the variations in distances between the lower lamina to upper lamina features (e.g., ridges and/or cross-ribs) owing to the former's local curvature. This variation reduction assisted the segmentation and classification of features on the upper lamina. The lower lamina was digitally removed from each 1D z -axis phase profiles before

running a PCA dimensionality reduction (5 principal components) on remaining upper lamina's 1D z-axis phase profiles, followed by feature vectorization using K-means clustering. We increased the number of clusters in the analysis based on the complexity and the reconstruction quality of the volume. For noisy and complex volumes, we manually labelled the K-means clusters further into ridges, cross-ribs, trabeculae and discarded obvious outliers.

After segmentation, the 1D curves classified based on the (non-exclusive) presence of the following features: lower lamina, ridges, cross-ribs, and trabeculae. Each of these upper and lower lamina features were separately fitted to 1D Gaussians to infer the average densities, z-axis width, and z-position of these features. These 1D Gaussian fits also reduced artifacts from tomographic stitching and noise. Where trabeculae occurred under a ridge (both features lying above a lower lamina) a triple Gaussian model was used. From these fits the area (phase sum) and the standard deviation (thickness t) was determined and then used to calculate the integrated electron density along the z-axis for each pixel at the x-y plane (52). With the electron density of a chitin monomer (e_{chitin}^-) and the x-ray wavelength (λ_x), we converted the phase sum into an estimate of the total number of chitin monomers. The mass density (ρ) of each component at a given pixel was calculated by using the molecular mass of a chitin monomer (m_{chitin}) and Avogadro's number (N_A) (Eq. 1).

$$\rho = \left(\frac{\varphi}{r_e \lambda_x t N_A} \right) \left(\frac{m_{chitin}}{e_{chitin}^-} \right) \quad (1)$$

We emphasize that our absolute mass density estimates obtained with PXCT are based on the average ratio of nucleons-to-electrons in chitin ($C_5H_{10}O_2N$) only, because the cuticular protein and pigment composition within the scales are unknown. Hence, estimates of absolute densities would increase by 11%, should we have recalibrated for melanin pigment monomers instead ($C_{18}H_{10}O_2N_2$). Nevertheless, the relative differences in the average mass densities between upper and lower laminae in all four scales in Fig. 4 exceed this 11% difference due to calibration choice. Consequently, the density differences between the most prominent features in the lower and upper laminae cannot be explained by a highly unlikely replacement of all chitin monomers entirely with melanin monomers.

Partial volume effect

The mass density estimations of the sub-structures should be inferred cautiously as they suffer from the partial volume effect, i.e., a limited resolution of an imaging system causes a loss in activity in smaller features. For example, the ectopic cuticular film of *B. anynana yellow* mutant scale is much thinner than a PXCT voxel; thus, the electron mass reported in that voxel is averaged over the larger voxel size instead of the actual thickness of the upper lamina, which causes a lower density than the actual value. Though significant in the case of the thin ectopic film, all the other features (cross-ribs, ridges, trabeculae, and lower lamina) that are larger than two voxels are less affected by the partial volume effect (53). *Conservatively, all the mass density values estimated should be considered as the lower bound of the actual densities.* However, the relative change in densities of sub-structures within a scale (except for the ectopic film) and densities of the same structure between different scales can be inferred with confidence since the voxel size is the same in all reconstructions. It is noteworthy that the partial volume effect can be substantially reduced by collecting PXCT data with a higher resolution (i.e., by increasing exposure times at the expense of longer data acquisition times); hence it is not an innate limitation of PXCT or the mass density estimation.

Optical modelling

The reflectance spectrum from a scale is a collective product of a series of optical responses from the structure. Numerical methods can simulate the complete response spectrum from a given 3D structure. However, they are computationally expensive for carrying out multiple simulations that is required for parameter tuning to fit the experimental response curves. Here we used an analytical model where an incident spectrum reflected back from the lower lamina at various layers interfere to produce a response reflection spectrum and the spectrum is further attenuated by a 1D phase grating (i.e., the upper lamina). We used the scattering matrix (S-matrix) method to calculate a reflectance spectrum from the lower lamina as we can model multi-layered lower lamina (N layers) with this method (54). Scattering matrix implementation in the PyPI python library has been used, and we calculated the reflection and transmission intensity (Eq. 2) for every wavelength data point from the experiment.

$$[I_{ref}(\lambda) I_{trn}(\lambda)] = S^{ll} (0, N) [I_{inc}(\lambda) 0] \quad (2)$$

For the upper lamina, we used a simple 1D transmission phase grating model (Eq. 3) (55). We calculate the diffraction pattern for every wavelength for given structural parameters, and the diffraction pattern is then integrated from $-\pi$ to π to get the response spectrum. Since the light reflected from the lower lamina is transmitted through the grating, the response spectrum from the S-matrix is used as the input spectrum for the phase grating model.

$$I = \int_{-\pi}^{\pi} (I_{ref}(\cos(\frac{\pi t_R}{\lambda}(n_{air} - n_R) + \frac{\pi p_R}{2\lambda}\theta))^2 \left(\left(\frac{\sin(N\frac{\pi p_R \theta}{\lambda})}{\sin(\frac{\pi p_R \theta}{\lambda})} \right) \left(\frac{\sin(\frac{\pi w_R \theta}{\lambda})}{\frac{\pi w_R \theta}{\lambda}} \right) \right)^2 d\theta \quad (3)$$

Parameters such as lower lamina thickness (t_L), inter-ridge spacing (p_R), ridge thickness (t_R) and window width (w_R) are measured experimentally from SEM and PXCT, but the thickness of each layer in the lower lamina and refractive indices (n_R, n_L) of them are unknown. We implemented a *Python* fitting routine that uses our optical model and the experimentally measured values as initial guesses to fit the experiment reflectance data.

Absorption spectrum and pigment concentration estimation

Spectrophotometer measures absorbance $A(\lambda, t)$ from the fraction of the light transmitted $T(\lambda, t)$ through a sample of thickness t as a function of the wavelength of incident light λ . This absorbance is shown in Eq. (4)

$$A(\lambda, t) = -\log_{10} T(\lambda, t) . \quad (4)$$

In the case of butterfly scales, this absorbance is affected by the *types* and *density* of light-absorbing pigments within the scale, as well as the scale's thickness. Hence, to compare the density of pigments within different regions of a scale (i.e., upper versus lower lamina) and between similar scales, we need to account for the corresponding thicknesses of pigment-containing features within the scale. Fortunately for us, this thickness information can be inferred from SEM and PXCT measurements.

The SEM cross sections of the four types of scales presented in this manuscript each show relatively little variations in the thickness of their lower lamina (Figures S3 and S4). Unlike the lower lamina, however, the upper laminae of each of these four scale types contain a complex structure with ridges, cross-ribs, trabeculae and window regions. Hence, the probability distribution of thicknesses across such a complex structure should be estimated for

its transmittance model. For each scale, we estimated the thickness distribution of its upper lamina from 100 randomly sampled 2 μm -diameter patches from its corresponding PXCT reconstruction volume. This diameter was chosen to match the illumination spot sizes using in the micro-spectrophotometry measurements (described in an earlier section in this SI).

Overall, the average transmittance for such an upper and lower lamina structure can be modelled using the following pair of Beer-Lambert law:

$$T_{U+L}(\lambda) = e^{-(\mu_L(\lambda)t_L)} \sum_{t_U} Pr(t_U) e^{-(\mu_U(\lambda)t_U)} \quad (5)$$

$$T_L(\lambda) = e^{-(\mu_L(\lambda)t_L)} \quad (6)$$

where $\mu_L(\lambda)$, $\mu_U(\lambda)$ and t_L , t_U are pairs of absorption spectra and thickness of the lower and upper lamina respectively. $Pr(t_U)$ is the probability distribution of the upper lamina thickness (from PXCT reconstruction), which allows us to account for the varying thicknesses of the upper lamina features in each scale. These thickness values t_L are calibrated based on the thickness of the lower lamina experimentally measured from the SEM, which is more precise than that from PXCT.

To reduce the partial volume effect from upper lamina feature thicknesses (t_U) inferred from PXCT, we found the scaling factor needed to match the lower lamina thicknesses between PXCT and SEM measurements for each scale. This butterfly-scale-dependent scaling factor was used to rescale each scale's upper laminae thickness distribution to minimize the partial volume effect.

Here's what we did, in detail. For each scale, whose lower-lamina thickness t_L we've measured via SEM, we fitted its measured lower-lamina-only absorbance $T_L(\lambda)$ to Eq. (6) to find the absorption spectra of just its lower lamina $\mu_L(\lambda)$. These fitted parameters were substituted into Eq. (5), together with the upper lamina thickness distribution $Pr(t_U)$ from PXCT (after correcting for partial volume effects), and fitted to the upper-plus-lower lamina microphotospectra absorbance $T_{U+L}(\lambda)$. Doing this gave us the absorption spectra of just the upper lamina $\mu_U(\lambda)$.

Notice that now that we have the thickness-independent absorption spectra of the upper and lower lamina (i.e., $\mu_U(\lambda)$ and $\mu_L(\lambda)$), we can determine the chemical signature and density of the pigments in each. To facilitate this, we decompose the absorption spectrum $\mu(\lambda)$ into two independent parts:

$$\mu(\lambda) = c\varepsilon(\lambda) \quad (7)$$

where c is the molar concentration of the light-absorbing pigments and $\varepsilon(\lambda)$ is the molar absorption spectrum of these pigments. Should the upper and lower lamina have the comparable wavelength dependence of $\varepsilon(\lambda)$ (i.e., $\varepsilon_U(\lambda)/\varepsilon_L(\lambda)$ is a wavelength-independent constant) we can be more confident in asserting that they contain the same *type* of pigments, except at different relative different concentrations. Figure S2 shows the molar absorption spectrum $\varepsilon(\lambda)$ for the upper and lower lamina of four scales studied here (that of the lower lamina of *Junonia* male is omitted because it is too noisy). Figure S2 also compares the relative molar concentrations of pigments in these scales assuming that the light-absorbing pigments are the same type in all scales.

Transmission electron microscopy of resin-embedded scales

Small pieces of each wing section were cut and fixed in 2.5% Glutaraldehyde in (Phosphate-buffered saline) PBS overnight at 4°C followed by three washes in PBS. Samples were then processed at the Electron Microscopy Unit at the Yong Loo Lin School of Medicine, NUS. Briefly, samples were post-fixed in 1 or 2% OsO₄, pH7.4 for 1 hour at room temperature under a fume hood and washed in deionized water for 10 minutes for 2 changes at room temperature. Dehydration was through an ascending ethanol series at room temperature: 25% ethanol for 5 minutes, 50% and 75% ethanol for 10 minutes, 95% and 100% ethanol for 20 minutes. Samples were then transferred to 100% acetone for 20 minutes, 2 times. Infiltration was with the following steps: a) 100% acetone : Araldite resin (3:1) for 30 mins at room temperature b) 100% acetone : Araldite resin (1:1) for 1 hour at room temperature c) 100% acetone : Araldite resin (1:6) for overnight at room temperature d) Pure Araldite resin for 30 minutes at room temperature then for 30 minutes in a 40°C oven e) Change to pure Araldite resin again for 1 hour in a 45°C oven f) Last change to pure Araldite resin for 1 hour in a 50°C oven. Finally, samples were embedded in fresh resin and allowed to polymerize for 24 hours in a 60°C oven.

Ultrathin sections were cut using a Leica Ultracut UCT Ultramicrotome (Leica Microsystems, Germany) and transferred to formvar coated grids. For the *Junonia orithya* samples grids were either left unstained or stained with lead citrate. For the *Bicyclus anynana* samples, all grids were stained with lead citrate. Images were acquired on a FEI Technai T12 Transmission Electron Microscopy (FEI, Thermo Fisher Scientific, U.S.A).

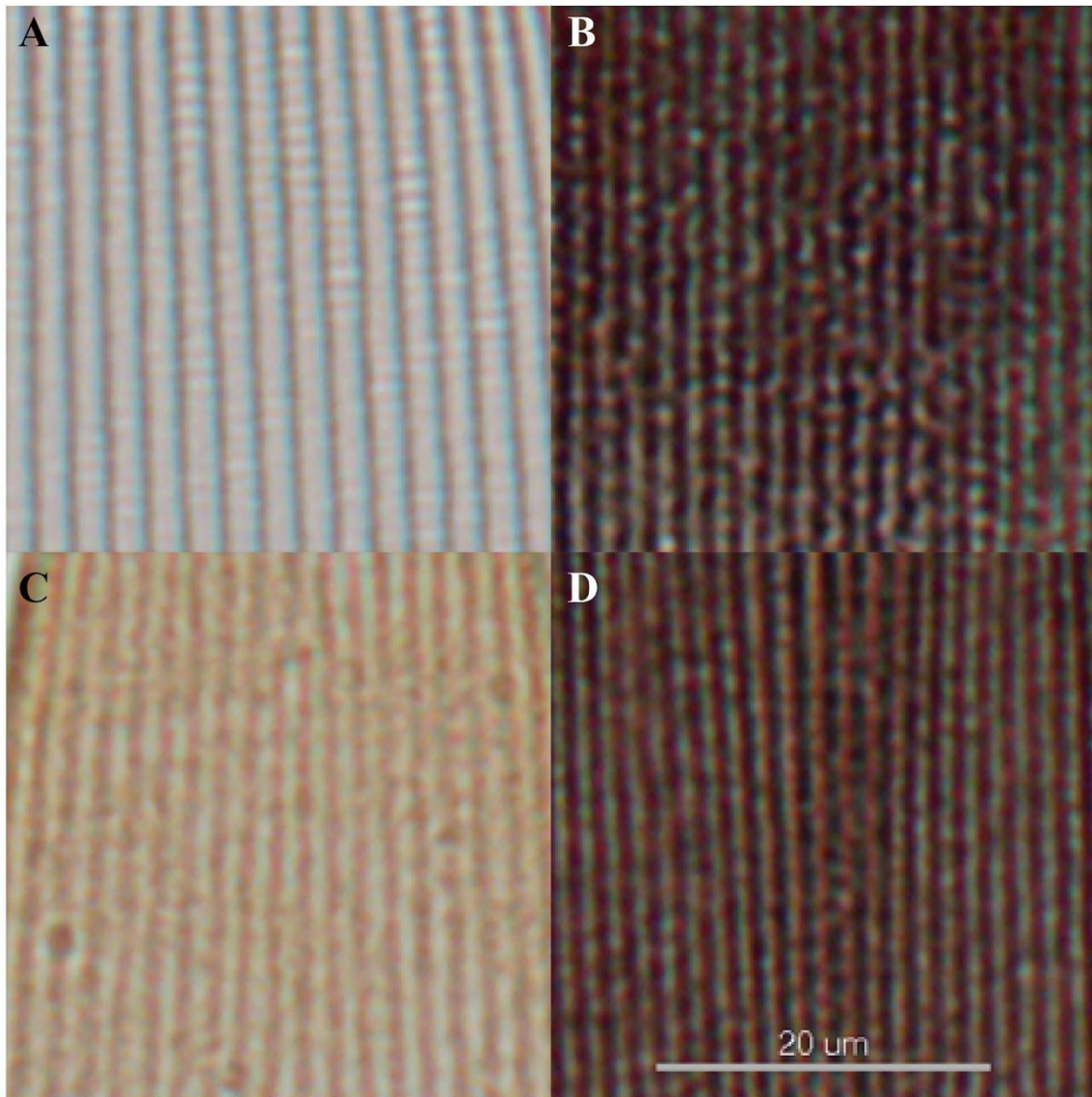


Fig. S1. Magnified optical microscopy images of *Junonia orithya* and *Bicyclus anynana* scales immersed in a refractive index matching liquid (clove oil). (A, B) *Junonia orithya* male blue scale (A) and female brown scale (B). (C, D) *Bicyclus anynana* yellow mutant scale (C) and wildtype scale (D). Immersion in a refractive index matching fluid removes the influence of structural colors and highlights the presence of pigments.

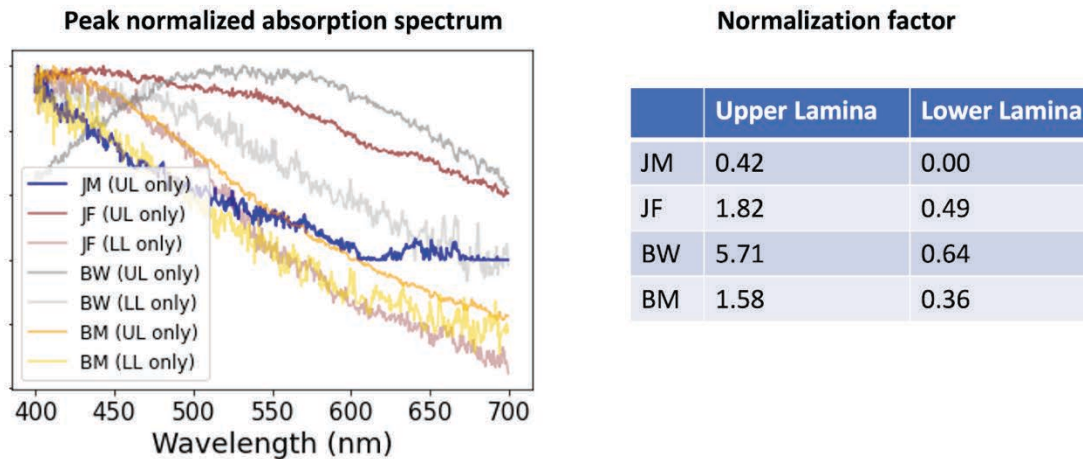


Fig. S2. Chemical signature and relative pigment density from the absorption spectra of upper and lower laminae of *Junonia orithya* and *Bicyclus anynana*. (Left) Absorption spectra are peak normalized to compare the shape which corresponds to their chemical signature. (Right) The corresponding normalization factors for the curves. When the chemical signatures of the scales are identical, the normalization factors represent their relative pigment densities. The peak normalized spectra show that chemical signatures of the scales are not identical, especially the upper lamina of *Bicyclus anynana* wildtype scale has a significantly unique spectral signature that has a peak around 500-550 nm. JM: *Junonia* male; JF: *Junonia* female; BW: *Bicyclus* wildtype; BM: *Bicyclus* yellow mutant

Bicyclus anynana

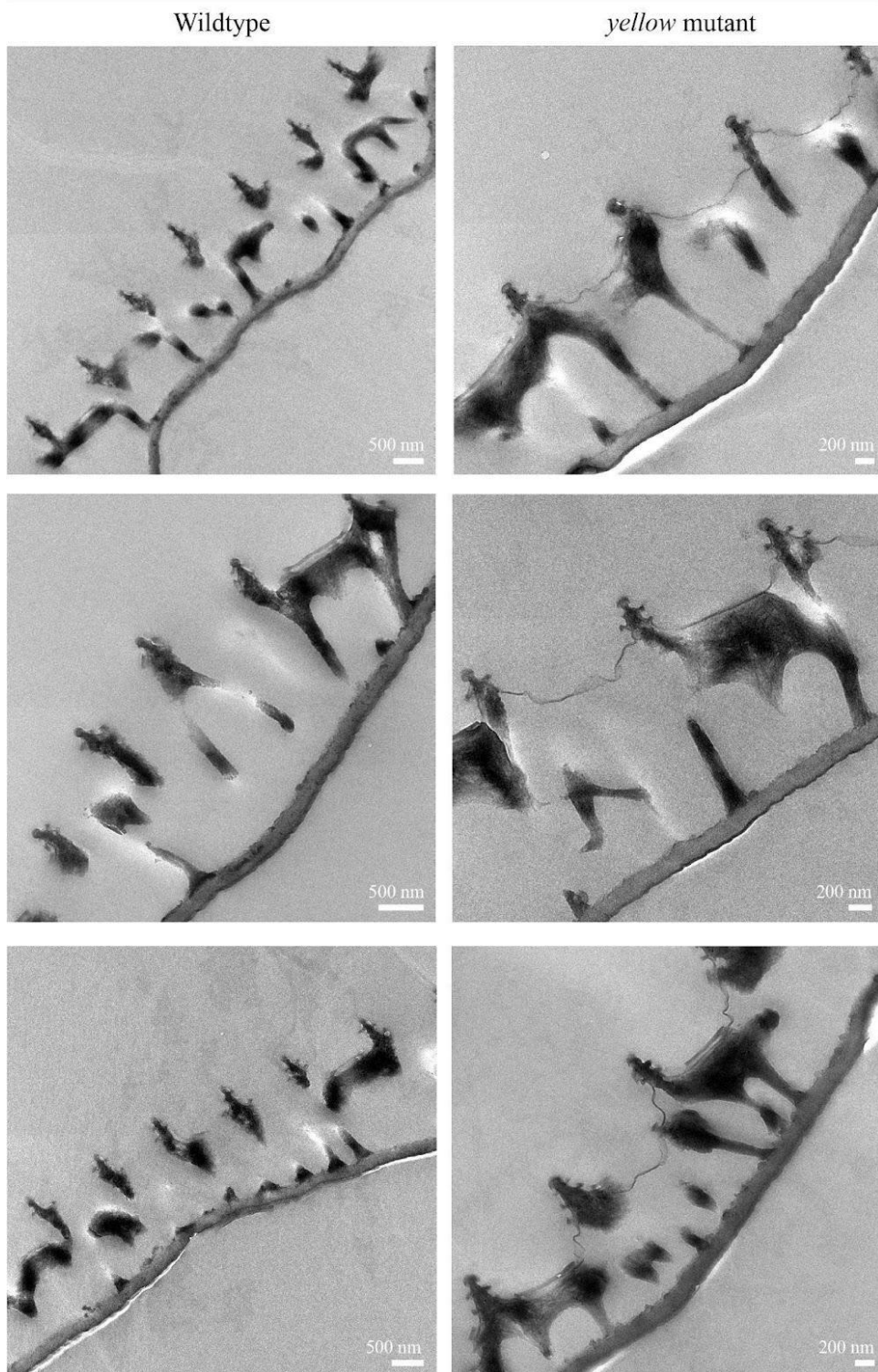


Fig. S3. TEM images of *Bicyclus anynana* Wildtype and *yellow* mutant scale cross-sections. The *yellow* mutant scales have a 10-20 nm thick ectopic cuticular film on the upper lamina, closing the windows.

Junonia orithya

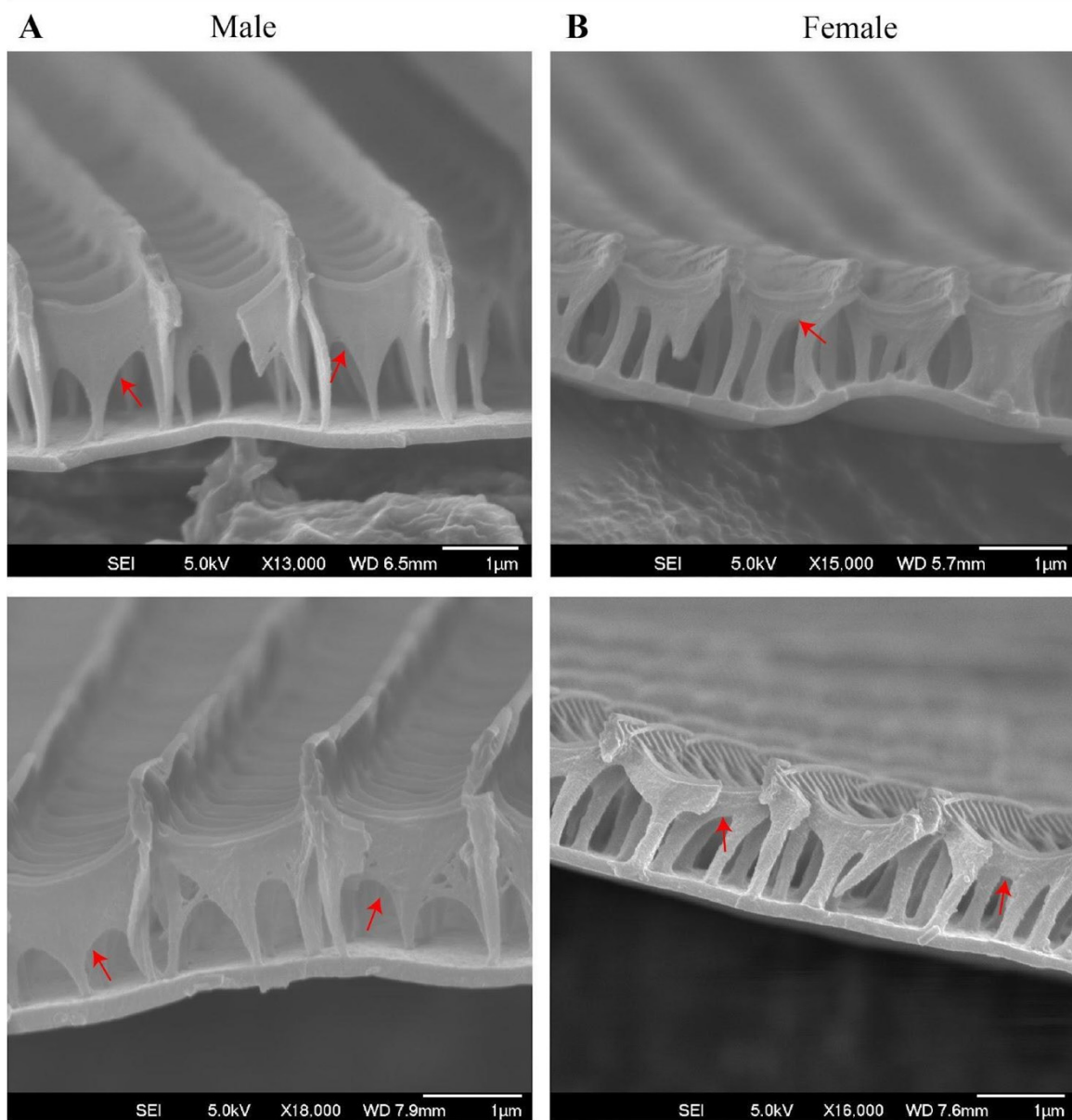


Fig. S4. Freeze-fractured SEM cross-sections of *Junonia orithya* male and female scales. Red arrows indicate the sheet-like extensions of the cross-ribs in male scales as compared to the less prominent extensions in the female scales.

Bicyclus anynana

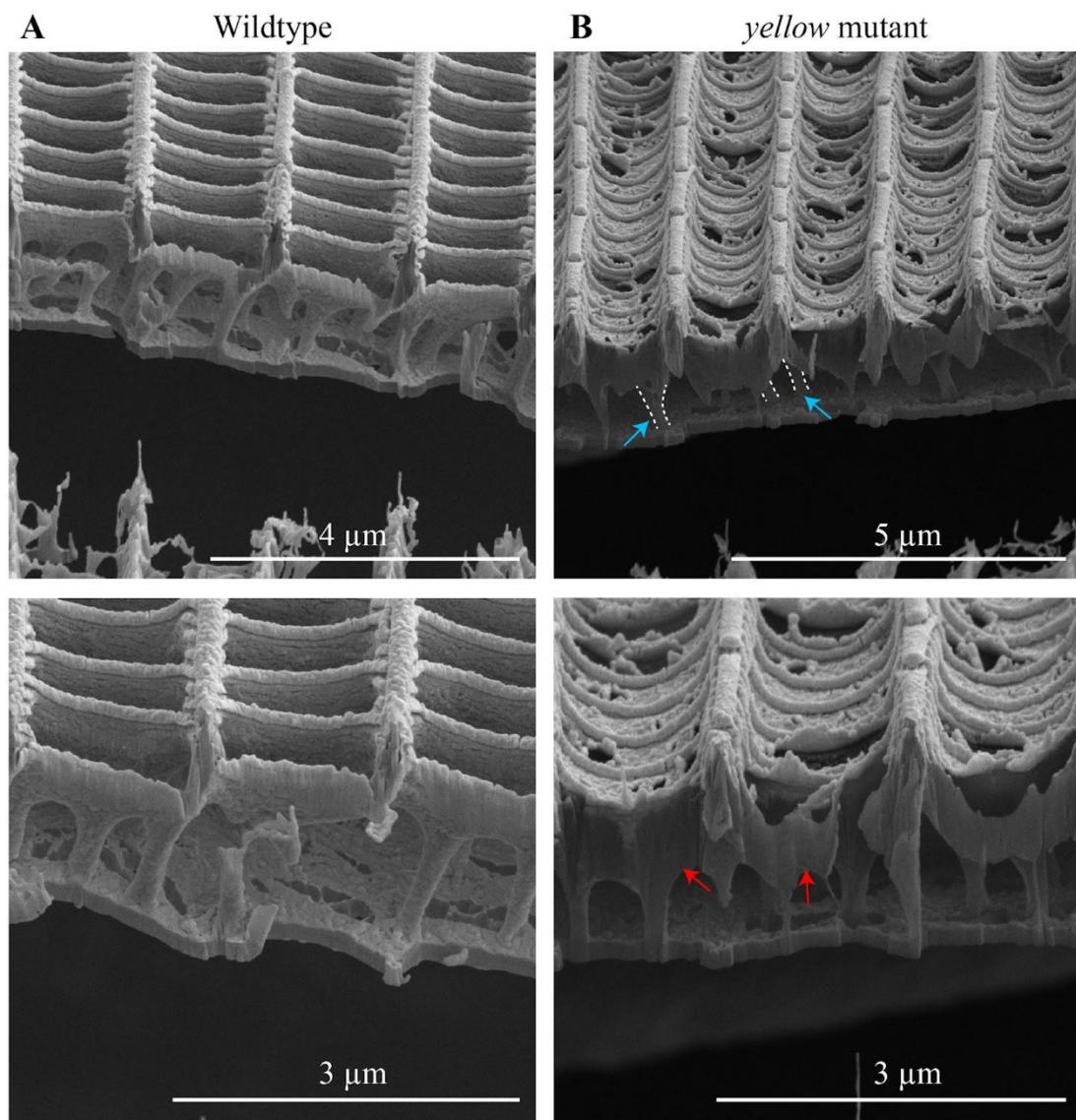


Fig. S5. FIB-SEM cross-sections of *Bicyclus anynana* Wildtype and *yellow* mutant scales. In the *yellow* mutant cross-sections (top) blue arrows and dotted white lines indicate curved trabeculae and (bottom) red arrows indicate sheet-like extensions of the cross-ribs that are absent

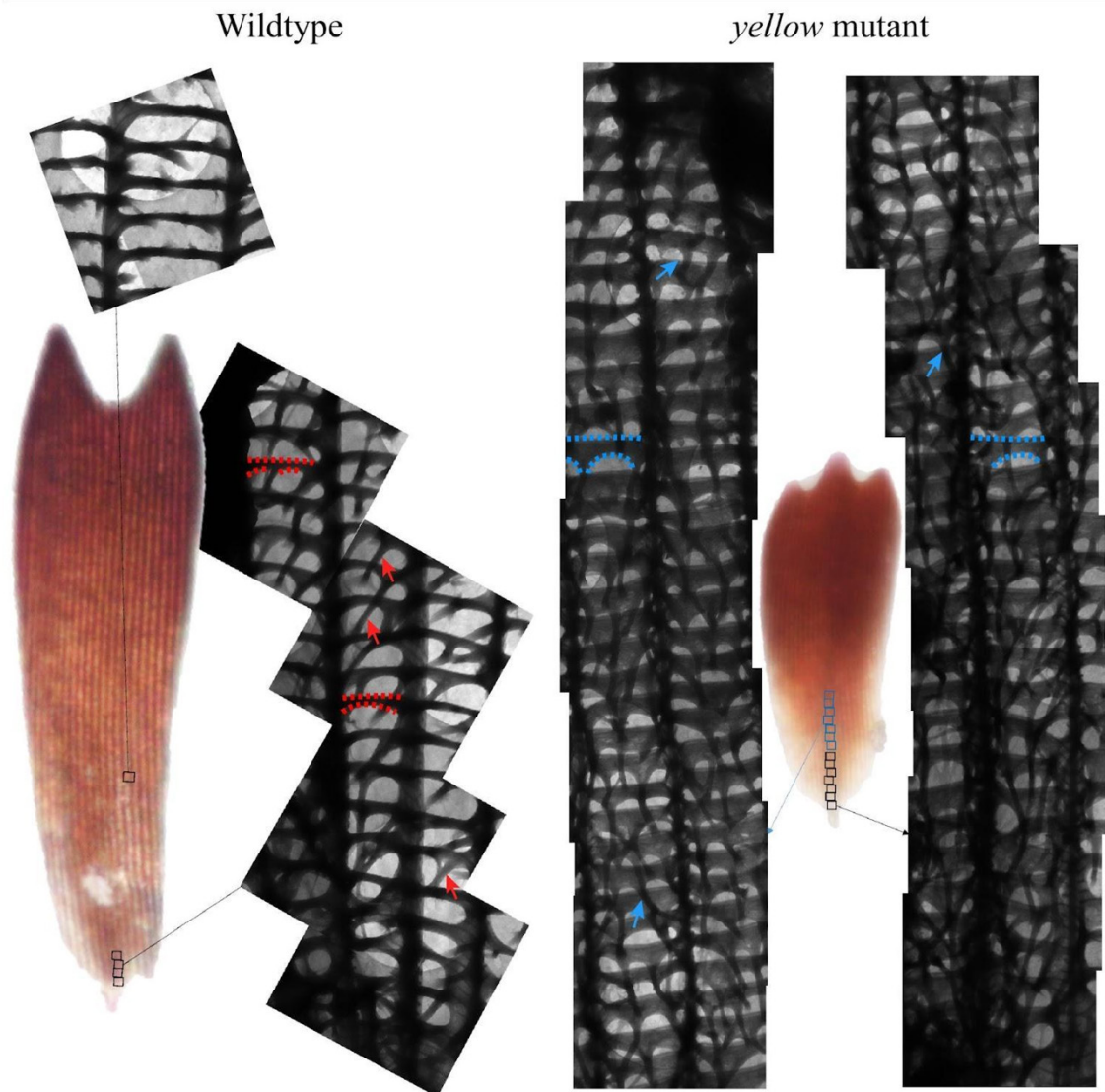


Fig. S6. TEM top-down images of *Bicyclus anynana* Wildtype and *yellow* mutant scales. Entire scales were directly mounted on Formvar-coated TEM grids and imaged. Images were taken in series at the different locations indicated by square boxes. Wildtype scales have thin cross-ribs (red dotted lines) with straight trabeculae (red arrows) extending to the lower lamina. In comparison to the Wildtype scales, *yellow* mutant scales have sheet-like extensions of the cross-ribs (blue dotted lines) and curved trabeculae (blue arrows).

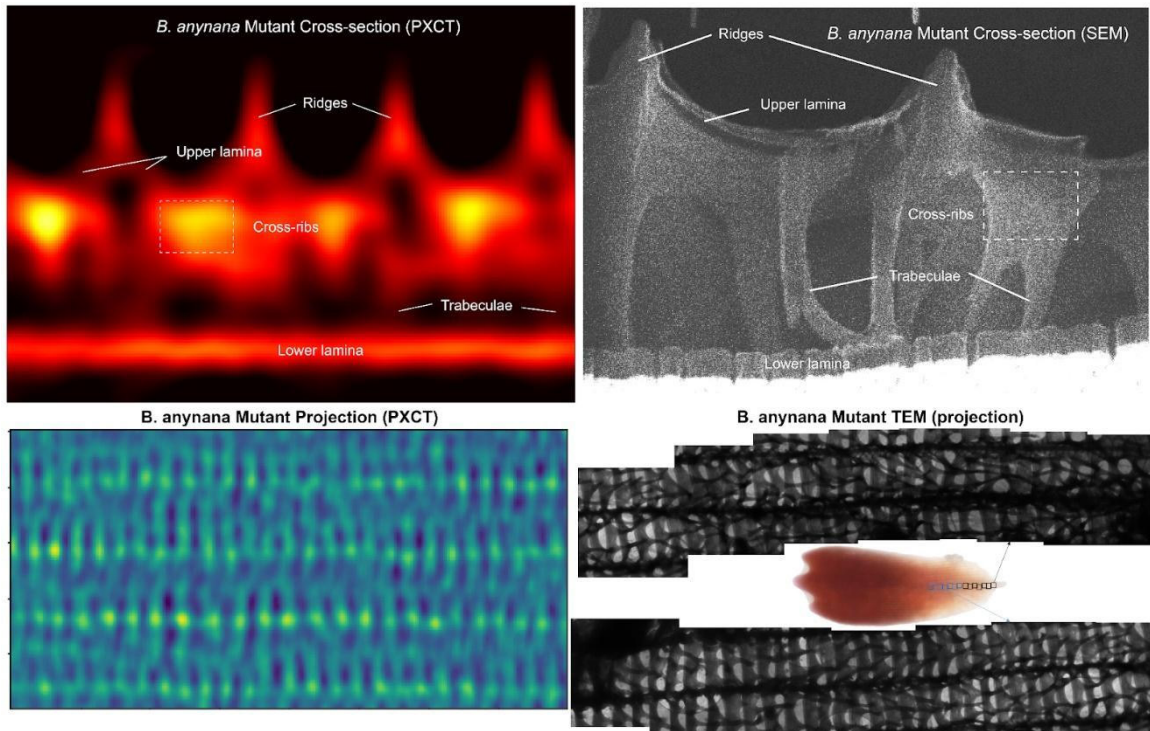


Fig. S7. PXCT cross-section and projection are compared with the SEM cross-section and TEM top-down images of *Bicyclus anynana yellow* mutant scale.

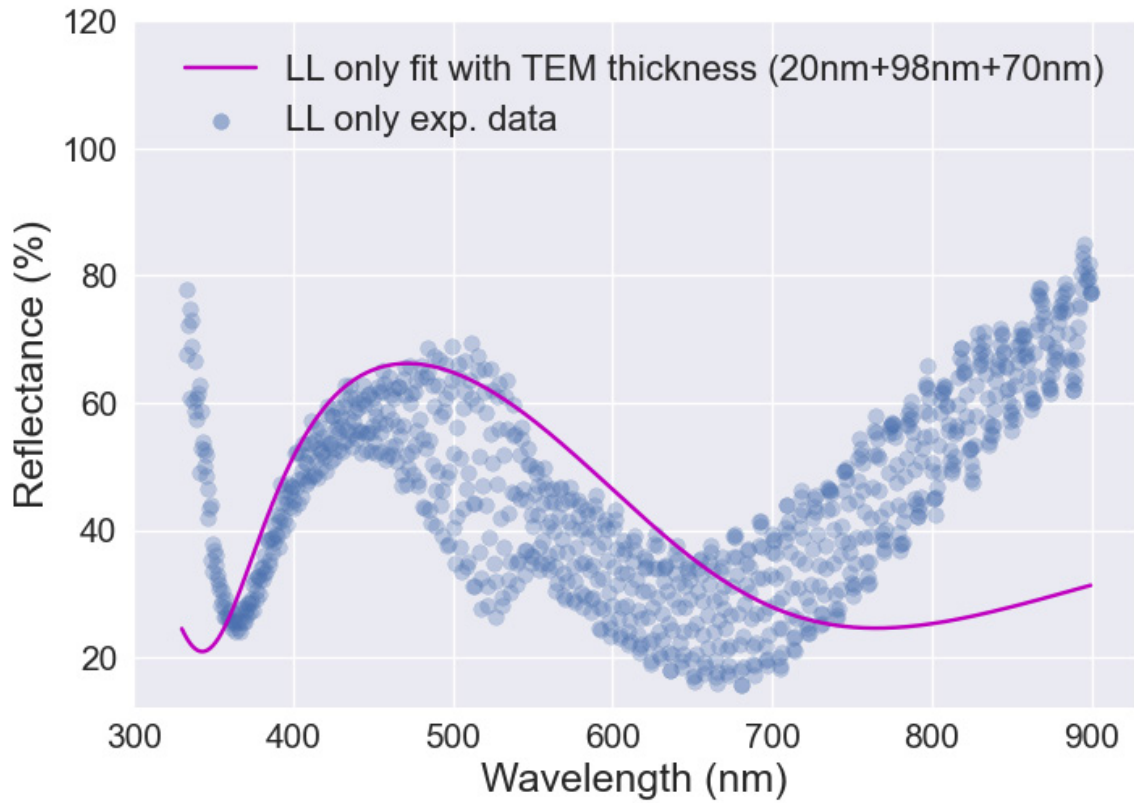


Fig. S8. The experimental reflectance spectrum of the lower lamina of a *J. orithya* male scale fit with the simulated spectrum based on the thickness values from the TEM image. The simulated reflectance spectrum was generated with the triple-layer thin-film interference model with the nominal thickness values of layers measured from the TEM image in Fig. 6B. The mismatch could arise from our model assuming a fixed refractive index for all wavelengths. LL only: Lower lamina only with the upper lamina physically removed.

Table S1.

Reflectance and absorbance spectra of *Junonia orithya* male blue and female brown scales and *Bicyclus anynana* wildtype and *yellow* mutant scales.

Table S2.

Inter-ridge distances, crossrib distances and lower lamina thickness of *Junonia orithya* male blue and female brown scales and *Bicyclus anynana* wildtype and *yellow* mutant scales.

Movie S1.

PXCT reconstruction of a *Junonia orithya* male blue scale.

Movie S2.

PXCT reconstruction of a *Junonia orithya* female brown scale.

Movie S3.

PXCT reconstruction of a *Bicyclus anynana yellow* mutant scale.

Movie S4.

PXCT reconstruction of a *Bicyclus anynana* wildtype black scale.

Movie S5.

Simulated color reflectance from the lower lamina of the *Junonia orithya* male blue scale and their abwing/adwing experimental reflectance micrographs overlaid with the lower lamina tilt map from the PXCT reconstruction of the same scale.